Nano Research
2020, 13(9): 2431–2437

ISSN 1998-0124 CN 11-5974/O4
https://doi.org/10.1007/s12274-020-2871-0

Research Article

Polymer matrix mediated solvation of $LiNO_3$ in carbonate electrolytes for quasi-solid high-voltage lithium metal batteries

Zijian Wang, Kai Yang, Yongli Song, Hai Lin, Ke Li, Yanhui Cui, Luyi Yang (✉), and Feng Pan (✉)

School of Advanced Materials, Peking University Shenzhen Graduate School, Shenzhen 518055, China

Received: 1 March 2020 / **Revised:** 17 April 2020 / **Accepted:** 10 May 2020

ABSTRACT

Lithium (Li) metal is one of the most promising anodes for next-generation energy storage systems. However, the Li dendrite formation and unstable solid-electrolyte interface (SEI) have hindered its further application. Lithium nitrate ($LiNO_3$) is extensively used as an effective electrolyte additive in ether-based electrolytes to improve the stability of lithium metal. Nevertheless, it is rarely utilized in carbonate electrolytes due to its low solubility. Here, a novel gel polymer electrolyte (GPE) consisting of poly(vinylidene fluoride) (PVDF), poly(methyl methacrylate) (PMMA), poly(ethylene oxide) (PEO) with $LiNO_3$ additive is proposed to solve this issue. In this GPE, polyether-based PEO serves as a matrix for dissolving $LiNO_3$ which can be decomposed into a fast Li-ion conductor (Li_3N) in conventional carbonate electrolytes to enhance the stability and Li^+ conductivity of the SEI film. As a result, dendrite formation is effectively suppressed, and a significantly improved average Coulombic efficiency (CE) of 97.2% in Li-Cu cell is achieved. By using this novel GPE coupled with Li anode and $LiNi_{0.5}Mn_{0.3}Co_{0.2}O_2$ (NMC532), excellent capacity retention of 94.1% and high average CE of over 99.2% are obtained after 200 cycles at 0.5 C. This work presents fresh insight into practical modification strategies on high-voltage Li metal batteries.

KEYWORDS

Li anode, gel polymer electrolyte, lithium nitrate, Li dendrite, electrolyte additives

1 Introduction

Lithium-ion batteries (LIBs) have made a huge success in the field of energy storage. However, the development of the LIBs, especially in the field of electric vehicles, has been impeded by the inferior theoretical specific capacity of graphite anode (372 $mAh \cdot g^{-1}$) [1–3]. Lithium (Li) metal anode, with extremely high theoretical specific capacity (3,860 $mAh \cdot g^{-1}$) and ideal electrochemical potential (−3.04 V vs. the standard hydrogen electrode), is regarded as a most promising anode material for next-generation high-energy-density batteries [4, 5], such as Li-S batteries [6], and Li-air batteries [7].

Nevertheless, the application of Li metal anode has been plagued by constant Li dendrite growth and low Coulombic efficiency (CE), leading to poor cycle stability and safety hazards. Extensive efforts have been devoted to addressing these intractable challenges, including artificial SEI [8, 9], threedimensional (3D) host [10–13], interlayers between Li and separator [14], electrolyte additives [15–17], highly concentrated electrolyte [18] and solid-state batteries (SSB) [19–22]. Among these strategies, electrolyte additives have attracted wide attention for its availability, economy, and effectiveness, which can construct a protective layer on Li anode *in-situ* to reinforce the unstable solid-electrolyte interface (SEI) film. At present, lithium nitrate ($LiNO_3$) has played an important role in inhibiting the "shuttle effect" of lithium polysulfides and stabilizes the Li dendrite growth in Li-S batteries [23, 24]. However, the low upper limit of the electrochemical window has restricted the application of ether electrolytes in high-voltage batteries. By contrast, carbonate electrolytes, such as ethylene carbonate (EC) and dimethyl carbonate (DMC), are widely used in high-voltage batteries for their wide electrochemical windows [25]. Nevertheless, the application of $LiNO_3$ in carbonate electrolytes has been greatly limited for its low solubility [26].

On the one hand, although liquid electrolytes (LE) in LIBs exhibits high ionic conductivity of 10 $mS \cdot cm^{-1}$ at ambient temperature for organic electrolytes [27], the problem of electrolyte leakage has posed a potential safety hazard. On the other hand, despite the improved safety features, solid polymer electrolytes are limited by their low ionic conductivities (below 10^{-6} $S \cdot cm^{-1}$) at ambient temperature [28–31]. Therefore, gel polymer electrolytes (GPE), such as poly(vinylidene fluoride) (PVDF), poly(methyl methacrylate) (PMMA), poly(ethylene oxide) (PEO), poly(acrylonitrile) (PAN), combining the merits of organic liquid electrolytes with solid polymer electrolytes, possess proper ionic conductivity, appreciable electrochemical window, and no leakage of liquid, has attracted widespread attention [32, 33].

Recently, many researchers have attempted to solve the application of $LiNO_3$ in carbonate electrolytes. Consequently, electrolyte additive of CuF_2, preimpregnating the $LiNO_3$ in glass fiber, and encapsulating $LiNO_3$ nanoparticles in porous PVDF were proposed [34–36]. Although these strategies have improved the performance of the batteries, they are either impractical or cumbersome and inevitably encountered traditional safety issues of LMBs. Here, we modified the pristine blended PVDF-PMMA (PV-PM) GPE by tactfully adding polyether-based PEO as a matrix for dissolving $LiNO_3$ (symbolized as PV-PM-PE-LN

Address correspondence to Luyi Yang, yangly@pkusz.edu.cn; Feng Pan, panfeng@pkusz.edu.cn

and the GPE without $LiNO_3$ symbolized as PV-PM-PE) and applied it to the high-voltage Li metal battery with carbonate electrolytes. As a result, due to the dissolution of $LiNO_3$ in PEO, a stable SEI film containing Li_3N fast ion conductor can be formed on the surface of Li metal, leading to a uniform Li deposition (as demonstrated in Fig. 1(a)). By contrast, due to the unstable SEI, severe Li dendrite growth can be observed at the interface between Li anode in the absence of $LiNO_3$ (as illustrated in Fig. 1(b)). By coupling PV-PM-PE-LN with EC/DMC electrolyte in a Li-$LiNi_{0.5}Mn_{0.3}Co_{0.2}O_2$ (NMC532) full cell, excellent capacity retention of 94.1% was obtained after 200 cycles (57.3% after 200 cycles for PV-PM-PE), and a high average Coulombic efficiency surpasses 99.2% was achieved at 0.5 C. This facile strategy can provide a new idea of electrolyte additive to achieve a dendrite-free Li anode as well as a safer high-voltage Li metal battery.

2 Experimental

2.1 Material preparation

PVDF (Solef, America), PMMA (M_W = 4 M, Acros), and PEO (M_W = 4 M, Dow Chemical Company) were dissolved in dimethylformamide (DMF, Alfa Aesar) at a mass ratio of 6:4:2, then certain amount of $LiNO_3$ (relative to total polymer mass) was added as an additive to the above sample followed by stirred at 70 °C for 12 h. the solution was cast on a Teflon mold using a 150 μm doctor blade and dried on an 80 °C hotplate for 24 h. After the solvent was evaporated, the membrane was peeled off and punched into disks with 19 mm in diameter and then transferred into a vacuum oven at 80 °C for at least 48 h before used. The obtained membrane was symbolized as PV-PM-PE-LN. The preparation of PV-PM-PE and PV-PM was similar to that of PV-PM-PE-LN. For PEO-$LiNO_3$, PEO and $LiNO_3$ were dissolved in acetonitrile at a mass ratio of 20:3 (EO/Li = 10.5) to simulate the dissolution of 2.5 wt.% of $LiNO_3$ in PV-PM-PE-LN. After stirring at 70 °C for 10 h, the solution was dropped on a PTFE plate, then placed at 80 °C hotplate for 24 h to remove the solvent. All the operations sensitive to moisture was carried out in an Ar-filled glovebox with H_2O and O_2 contents below 5 ppm. The cathode was prepared by mixing NMC532, acetylene black, and PVDF binder with a weight ratio of 80:10:10 in N-methyl-2-pyrrolidone (NMP, Aladdin). The homogeneous slurry was coated on carbon-coated aluminum foil (15 μm in thickness) with a doctor blade and dried in a vacuum oven at 80 °C for 24 h to remove the remaining solvents. And then, the electrode materials were punched to disks with 10 mm in diameter, and the areal loading of active material is approximately 4 mg·cm^{-2}. 1.0 M $LiPF_6$ in EC/DMC electrolyte was used to immerse the dry polymer for 10 h, then take out the GPE and wiped off carefully with a clean wiper.

2.2 Electrochemical measurements

Lithium metal plate was purchased from China Energy Co., Ltd. All the electrochemical tests were carried out with a two-electrode cell configuration using CR2032 coin-type cell at 25 °C and assembled in an Ar-filled glove box with O_2 and H_2O contents below 0.1 ppm. For CE tests, Cu foil was adopted as the working electrode and the Li metal plate as the counter/reference electrode. First, 5 mAh·cm^{-2} Li source was deposited on the Cu substrate at a current density of 0.5 mA·cm^{-2}. Then 0.5 mAh·cm^{-2} Li was stripped and plated repeatedly at a current density of 0.5 mA·cm^{-2} for 18 cycles. Finally, the remaining Li was stripped at 0.5 mA·cm^{-2} to 1 V vs. Li/Li$^+$ and the CE was calculated according to the method expounded in former literature [37]. The Li/NMC532 full cells were tested within a voltage range of 3.0–4.3 V vs. Li/Li$^+$ with NEWARE multichannel battery testing system (Shenzhen NEWARE Electronics Co., Ltd.). The Li plating/striping tests were executed on Li/Li symmetrical cells at a current density of 0.5 and 1 mA·cm^{-2} with a specific areal capacity of 0.5 mAh·cm^{-2} and 1 mAh·cm^{-2}, respectively. The electrochemical impedance spectroscopy (EIS) was carried out with the range of 10^6 Hz to 1 Hz, and cyclic voltammetry (CV) data were obtained at the voltage range of 0–2.5 V vs. Li/Li$^+$ at a scan rate of 0.2 mV·s^{-1}. The above two tests are all completed in a Solartron 1470E electrochemical workstation (Solartron Analytical, UK). The linear sweep voltammetry (LSV) was performed in Li/GPE/stainless steel (SS) cells with a scan range of 3–7 V vs. Li/Li$^+$ at a scan rate of 1 mV·s^{-1}.

2.3 Material characterization

The ionic conductivities of GPE were measured using EIS in a symmetrical SS/GPE/SS cell, which can be calculated by the following Eq. (1)

$$\sigma = \frac{l}{R_b S} \tag{1}$$

where R_b is the bulk resistance, S is the area of the blocking stainless steel electrodes, and l is the thickness of the GPE measured by micrometer caliper.

The absorbility of the polymer was measured according to the following steps. After weighing, the polymer was immersed in the liquid electrolyte for 5 h. The saturated GPE was then removed from the electrolyte and wiped carefully with a clean wiper. The absorbility (η) can be calculated according to the Eq. (2)

$$\eta = \frac{m_1 - m_0}{m_0} \times 100\% \tag{2}$$

where m_0 is the weight of pristine polymer and m_1 is the weight of polymer after soaked in the liquid electrolyte.

The morphology of the Li metal anodes surface was characterized via scanning electron microscopy (SEM; Zeiss SUPRA55). The X-ray photoelectron spectroscopy (XPS) analysis was conducted on an ESCALAB 250XL instrument in a scan

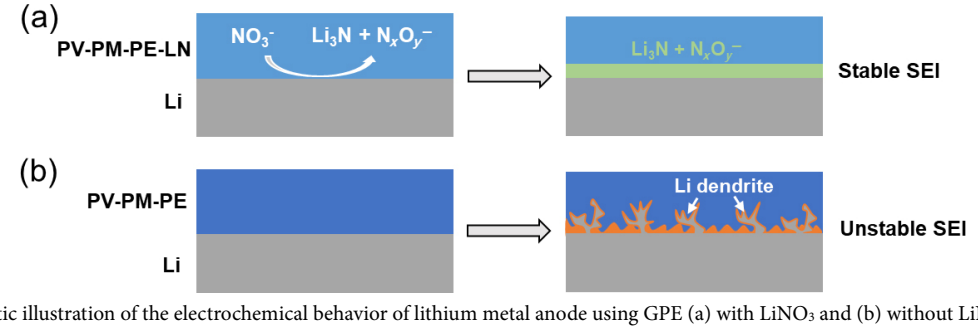

Figure 1 Schematic illustration of the electrochemical behavior of lithium metal anode using GPE (a) with $LiNO_3$ and (b) without $LiNO_3$.

step of 0.1 eV after etching 240 s. The X-ray diffraction (XRD) was performed on the Bruker D8 Advance powder X-ray diffractometer with 2θ in the range of 10°–80° with a step size of 0.02°·s^{-1} covered with a polyimide film.

3 Results and discussion

3.1 Material characterization

The conductivity of PV-PM-PE-LN would decrease with increasing mass fraction of $LiNO_3$, which could be ascribed to the increase of salt concentration leading to the increase of ion pairs formed by ion association (shown in Fig. 2(a)) [38]. Therefore, to balance the gain and loss brought by $LiNO_3$, 2.5 wt.% of $LiNO_3$ was chosen for all tests. To confirm whether the $LiNO_3$ was fully dissolved, XRD tests were proceeded on the $LiNO_3$, PV-PM-PE-LN, and PV-PM-PE, and the results are compared in Fig. 2(b). The XRD patterns of PV-PM-PE-LN exhibit the same diffraction peaks with PV-PM-PE without showing the peak of $LiNO_3$, suggesting the $LiNO_3$ additive has been completely dissolved in the GPE. Next, EIS was conducted on a SS/PEO-$LiNO_3$/SS cell at 80 °C (Fig. S1 in the Electronic Supplementary Material (ESM)), the measured conductivity of PEO-$LiNO_3$ is 0.95×10^{-6} S·cm^{-1}, which is attributed to the dissociation of $LiNO_3$, but the conductivity is limited by the ion contact interactions, as suggested in the previous report [39], proving that $LiNO_3$ is well dissolved in PEO. As shown in Fig. S2 in the ESM, PV-PM-PE-LN shows a thickness of 28 μm with a smooth surface and no obvious pinholes (Fig. S3 in the ESM), according to the experimental calculation, η is approximate to 126.5%. Arrhenius plots in Fig. S4(a) in the ESM exhibits that the ionic conductivity of PV-PM-PE-LN and PV-PM-PE is 8.77×10^{-4} and 9.22×10^{-4} S·cm^{-1} at 30 °C, respectively. The Nyquist plots of two GPEs tested at 30 °C show the impedance of PV-PM-PE-LN is slightly higher than PV-PM-PE (Fig. S4(b) in the ESM). Figure S5 in the ESM exhibits the electrochemical stability of the GPE, the current response in PV-PM-PE-LN increased significantly with lower voltage hysteresis compared to the PV-PM-PE, inferring rapid reaction kinetics for Li plating. Since the anodic stability of GPE also has an important effect on the performance of Li metal battery, linear sweep voltammetry (LSV) was carried out on Li/GPE/SS cells. Figure S6 in the ESM shows the upper voltage limit of PV-PM-PE-LN is up to 4.6 V vs. Li/Li$^+$, which is sufficient for high-voltage applications.

3.2 Lithium stripping/plating behaviors

The stability of SEI and the compatibility of electrolytes with Li metal electrodes play a vital role in electrochemical performances of lithium metal batteries, which could be analyzed by applying galvanostatic Li plating/striping cycling tests in Li/Li symmetric cells, and the pristine PV-PM was also joined for comparison. Figure 3(a) shows the time-dependent voltage curves of the Li/Li symmetric cell in EC/DMC based liquid electrolytes at a 0.5 mA·cm^{-2} with a capacity of 0.5 mAh·cm^{-2}. The Li/ PV-PM-PE-LN /Li cell exhibits a stable voltage polarization of 50 mV over 500 h of cycling without short-circuiting, whereas the cells using PV-PM-PE and PV-PM display higher polarization voltage of 61 and 68 mV, and short-circuited after 380 and 230 h, respectively. The EIS measurements show the comparison of interfacial resistance of the Li/Li symmetric cells after 50 cycles (Fig. S7 in the ESM), which explains the lowered voltage polarization despite PV-PM-PE-LN shows a lower ionic conductivity. It can also be seen from Fig. S8 in the ESM that using PV-PM-PE, the morphology of Li anode after 50 cycles shows uneven surface and massive dendrite with cracking, in sharp contrast, the surface of Li anode with PV-PM-PE-LN exhibits a smooth and dense morphology.

When the applied current densities increased to 1 mA·cm^{-2} with a capacity of 1 mA·cm^{-2}, the Li/ PV-PM-PE-LN/Li cell exhibited good cycling life up to 200 h, on the contrary, the cells using PV-PM-PE and PV-PM have short-circuited after only 87 and 46 h of cycling (Fig. S9 in the ESM), respectively. Moreover, as shown in Fig. 3(b), the CE was estimated using the method proposed by Zhang and co-workers [37]. The average CE of the Li-Cu cell using PV-PM-PE-LN achieves 97.2% at a current density of 0.5 mA·cm^{-2}, which is much higher than that of PV-PM-PE (87.9%) and PV-PM (74.3%). Li-Cu cell with a high CE represents less consumption of Li and electrolytes caused by side reactions, resulting in a smaller interface impedance (Fig. 3(c)). Consequently, it is speculated that the use of PV-PM-PE-LN could contribute to a more stable SEI with the rapid transport of Li$^+$.

To uncover the impact of $LiNO_3$ on the formation of SEI. XPS analyses were carried out after one cycle of CV to probe the chemical compositions of the SEI. In the F 1s spectra (Fig. 4(a)), the peaks at 684.4 and 686.6 eV can be assigned to the $-CF_3$ and LiF, respectively. For the PV-PM-PE-LN, it shows a weaker peak intensity of $-CF_3$ than that of PV-PM-PE. When the main component of the SEI film is LiF, the growth of lithium dendrites can be blocked more effectively, as pointed out by former researchers that the LiF-rich SEI can reduce the side reaction decomposition of organic electrolytes and hinder the dendrite formation [40]. Figure 4(b) shows that for the SEI film formed by PV-PM-PE-LN, there are three peaks at 393.8, 398.6, and 403.2 eV in the N 1s spectra, corresponding to RNO_2, Li_3N, and $LiNO_2$, respectively. Whereas these peaks cannot be observed in the absence of $LiNO_3$. It has long been known that the Li_3N possesses superior ionic conductivity, which can

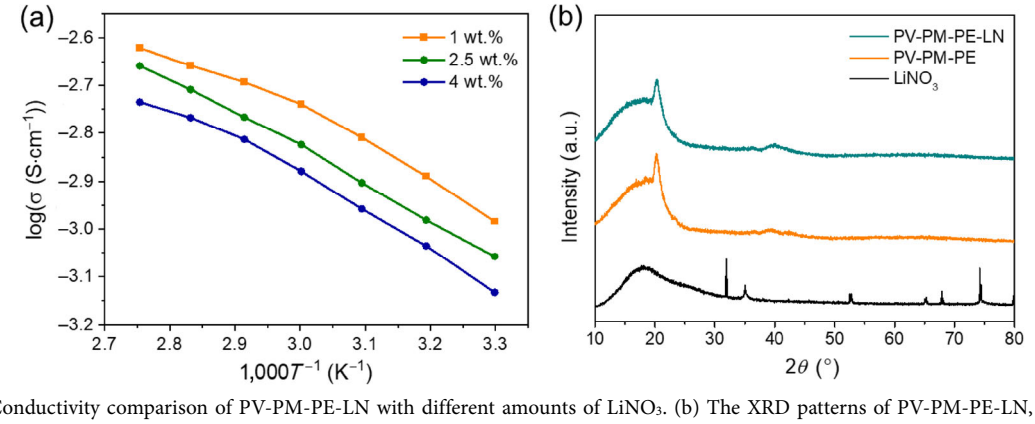

Figure 2 (a) Conductivity comparison of PV-PM-PE-LN with different amounts of $LiNO_3$. (b) The XRD patterns of PV-PM-PE-LN, PV-PM-PE, and $LiNO_3$, respectively.

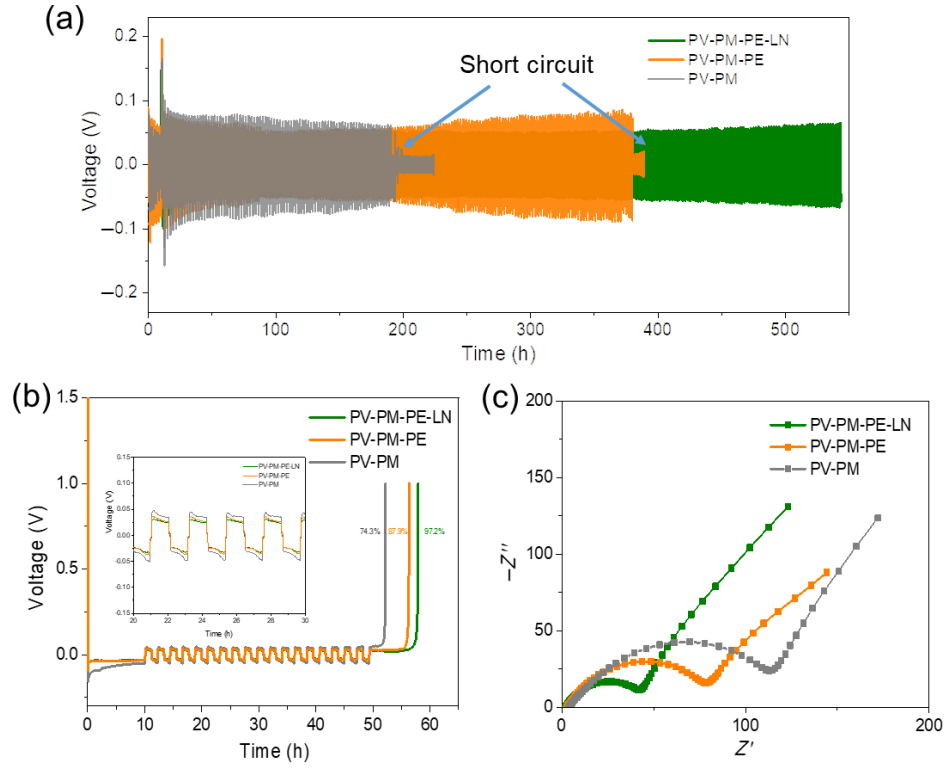

Figure 3 (a) The voltage–time profiles of Li symmetrical cells at a current density of 0.5 mA·cm^{-2} with a capacity of 0.5 mAh·cm^{-2}. (b) Voltage versus time plot to determine the average CE of lithium metal anode at a current density of 0.5 mA·cm^{-2}. (c) Nyquist plots of the Li/Cu cells after CE test.

enhance the interfacial ion migration as well as the stability of the SEI [34–36, 41]. In the Li 1s spectrum, an additional Li–N peak is observed in 55.5 eV (Fig. S10 in the ESM), signifying the existence of Li_3N and $N_xO_y^-$. Also, the peak intensity of –$ROCO_2Li$ in PV-PM-PE is stronger than that in PV-PM-PE-LN, which further confirms the excessive decomposition of electrolyte in PV-PM-PE due to the SEI instability.

From the results above, it can be inferred that the robust SEI film can be ascribed to the decomposition of $LiNO_3$. According to the mentioned in the literature, when the applied potential is under 1.6 V, $LiNO_3$ can be reduced on the surface of Li anode to form SEI that containing Li_3N under the condition of ether electrolytes [19, 20], which could stabilize not only the Li anode but also suppress the reduction of the polysulfide in the Li anode. To explore further insight mechanism of the SEI film formation, the CV test was employed in Li/Cu cells, and a voltage range of 0–2.5 V vs. Li/Li^+ was applied at a scan rate of 5 mV·s^{-1} (Fig. S11 in the ESM). Compared with PV-PM-PE, an additional reduction peak at 1.42 V was observed in PV-PM-PE-LN, which verifies the reduction of $LiNO_3$.

The effect of $LiNO_3$ on the morphology of plated Li on Cu is also investigated. In contrast with the needle-like dendritic structured Li formed in the presence of PV-PM-PE, spherical Li was obtained with PV-PM-PE-LN (Figs. 4(c) and 4(d), Fig. S12 in the ESM). When the applied current density is changed to 0.2 mA·cm^{-2} with the capacity of 2 mAh·cm^{-2}, mossy-like Li dendritic deposition formed on Cu in the presence of PV-PM-PE. By contrast, Li prefers to deposit into a smooth and uniform morphology with PV-PM-PE-LN (Figs. 4(e) and 4(f)). Therefore, ameliorating the SEI film by modifying the composition of the GPE can have a significant influence on the morphology of lithium deposition. Li_3N formed by the decomposition of $LiNO_3$ in PV-PM-PE-LN not only has high ionic conductivity but also can stabilize SEI film, contributing to reconstructing the interface between Li anode and electrolytes. These exceptional features conduced to the rapid and uniform striping/plating of Li.

3.3 Battery performance

In order to evaluate the electrochemical performances of PV-PM-PE-LN/PV-PM-PE in the practical battery system, both PV-PM-PE-LN and PV-PM-PE were coupled Li metal anode with NMC532 cathode. As shown in Fig. 5(a), the Li/NMC532 full cell with a PV-PM-PE-LN delivers higher capacity retention of 94.08% compared with PV-PM-PE (57.31%) after 200 cycles at 0.5 C. Furthermore, the CE of the Li/NMC532 full cell with PV-PM-PE-LN is relatively stable with an average CE as high as 98%, whereas the Li/NMC532 cell with PV-PM-PE shows a poor average CE of 85% and fluctuates with cycling. The voltage profiles of the 50th cycle and 120th cycle (Fig. 5(b)), show that at the beginning of the 50th cycle, the polarization voltage of Li/NMC532 cell with PV-PM-PE is slightly higher than that with PV-PM-PE-LN. However, its capacity declined rapidly and showed an unusually high polarization voltage at the 120th cycle. Compared with PV-PM-PE, PV-PM-PE-LN shows better cycle performance even at a high rate of 2 C (Fig. S13 in the ESM). The poor capacity retention and high polarization voltage of PV-PM-PE can be ascribed to the unstable and growing SEI. EIS measurements of the Li/NMC532 full cell with 0.5 C were also performed to examine the kinetic features between the electrode and electrolyte. The Li/NMC532 cell with PV-PM-PE-LN exhibits a lower impedance of 17 Ω after 100 cycles (in contrast, 33 Ω for PV-PM-PE; Fig. S14 in the ESM). The rate capability of the two cells is also investigated at the C-rates from 0.2 to 4 C, and the results are shown in Fig. 5(c). For the cell using PV-PM-PE-LN, an average specific capacity of 167.27, 153.78, 136.01, 117.47, and 88.94 mAh·g^{-1} was obtained at the C-rates of 0.2, 0.5, 1.0, 2.0, and 4 C, respectively. When the C-rate was reverted to 0.2 C again, a capability of 165 mAh·g^{-1} can be recovered, exhibiting good cycling stability and reversibility. In comparison, at the same C-rates, the cell using PV-PM-PE delivered lower capacities (164, 148.2, 120.9, 87.75,

and 44.6 mAh·g^{-1}), especially when reaches a high rate of 4 C. Figure 5(d) shows the charge/discharge voltage profiles of the Li/PV-PM-PE-LN/NMC532 cell at different C-rates, which exhibit lower voltage polarization compared to the cell with PV-PM-PE (Fig. S15 in the ESM). Table S1 in the ESM shows the comparison chart of the performance with various reported GPE in LIBs. The superior performance of batteries delivered by PV-PM-PE-LN can be attributed to the following two

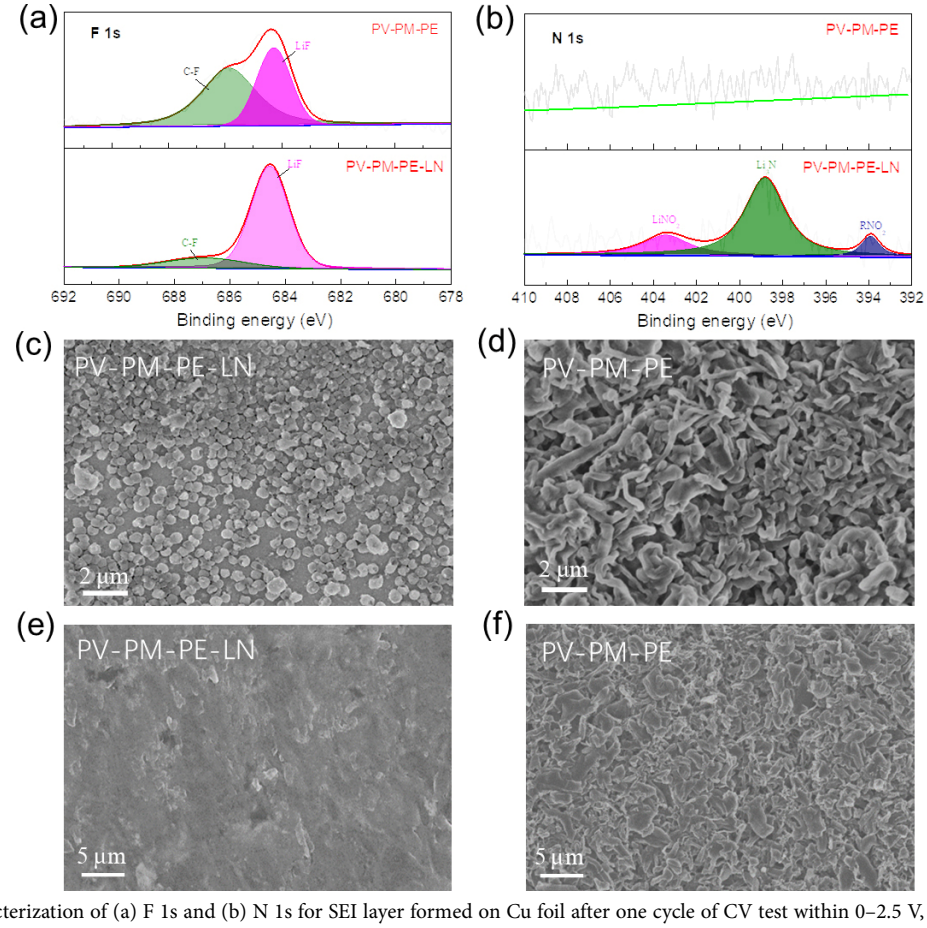

Figure 4 XPS characterization of (a) F 1s and (b) N 1s for SEI layer formed on Cu foil after one cycle of CV test within 0–2.5 V, (c) PV-PM-PE-LN and (d) PV-PM-PE at a current density of 0.1 mA·cm^{-2} with a capacity of 0.5 mAh·cm^{-2}, (e) PV-PM-PE-LN and (f) PV-PM-PE at a current density of 0.2 mA·cm^{-2} with a capacity 2 mAh·cm^{-2}.

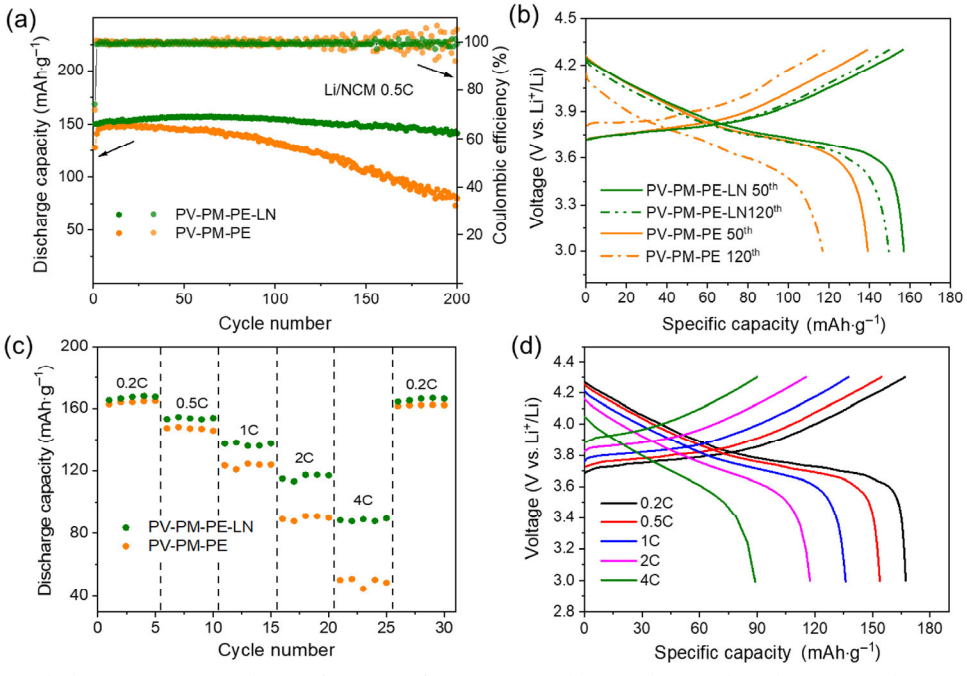

Figure 5 Electrochemical characterization. Cycling performance of Li/NMC532 cells in carbonate electrolyte. (a) Discharge capacities and CE of Li/NMC532 cells at 0.5 C. (b) Voltage profiles of Li/NMC532 cells. (c) Rate capability of Li/NMC532 cells. (d) Discharge/charge curves of Li/NMC532 cells at different current densities with the PV-PM-PE-LN.

reasons: On the one hand, Li_3N in SEI film formed by decomposition of $LiNO_3$ has high ionic conductivity, which will lead to lower polarization; on the other hand, more inorganic components in SEI can improve the stability and compactness of SEI film, reduce the side reaction, and stabilize the interface between Li anode and electrolyte.

4 Conclusions

In summary, a novel GPE consisting of PVDF, PMMA, PEO, and $LiNO_3$ is proposed for carbonate-based electrolyte, where the PEO serves as a matrix for dissolving $LiNO_3$. As a result, a stable SEI film containing Li_3N is obtained, ascribed to the reduction of NO_3^- around 1.42 V vs. Li/Li^+ in carbonate electrolytes. The stable SEI film brings about dendrite-free Li deposition with lowered polarization voltage. In addition, an improved average CE of 97.2% in EC/DMC electrolytes is obtained in a Li-Cu cell (in contrast to 87.9% for PV-PM-PE and 74.3% for PV-PM), and relatively smooth Li deposition morphology is observed. When the prepared PV-PM-PE-LN was coupled with high-voltage cathode NMC532, excellent capacity retention of 94.1% and high average CE of 99.2% were achieved after 200 cycles compared to the poor electrochemical performances of PV-PM-PE (57.3% of capacity retention, 85.1% of average CE). By utilizing the chemical property of PEO, a facile approach is proposed to employ $LiNO_3$ as an additive in carbonate electrolytes, which provides fresh prospectives on the electrolyte modification strategies.

Acknowledgements

This work was financially supported by National Key R&D Program of China (No. 2016YFB0700600), Soft Science Research Project of Guangdong Province (No. 2017B030301013), and Shenzhen Science and Technology Research Grant (No. ZDSYS201707281026184).

Electronic Supplementary Material: Supplementary material (additional SEM, XPS and electrochemical characterizations) is available in the online version of this article at https://doi.org/10.1007/s12274-020-2871-0.

References

[1] Lu, J.; Chen, Z. W.; Pan, F.; Cui, Y.; Amine, K. High-performance anode materials for rechargeable lithium-ion batteries. *Electrochem. Energy Rev.* **2018**, *1*, 35–53.

[2] Tarascon, J. M.; Armand, M. Issues and challenges facing rechargeable lithium batteries. *Nature* **2001**, *414*, 359–367.

[3] Du, H. R.; Huang, K. F.; Li, M.; Xia, Y. Y.; Sun, Y. X.; Yu, M. K.; Geng, B. Y. Gas template-assisted spray pyrolysis: A facile strategy to produce porous hollow Co_3O_4 with tunable porosity for high-performance lithium-ion battery anode materials. *Nano Res.* **2018**, *11*, 1490–1499.

[4] Liu, T. C.; Lin, L. P.; Bi, X. X.; Tian, L. L.; Yang, K.; Liu, J. J.; Li, M. F.; Chen, Z. H.; Lu, J.; Amine, K. et al. *In situ* quantification of interphasial chemistry in Li-ion battery. *Nat. Nanotechnol.* **2019**, *14*, 50–56.

[5] Xiang, J. W.; Yang, L. Y.; Yuan, L. X.; Yuan, K.; Zhang, Y.; Huang, Y. Y.; Lin, J.; Pan, F.; Huang, Y. H. Alkali-metal anodes: From lab to market. *Joule* **2019**, *3*, 2334–2363.

[6] Yin, Y. X.; Xin, S.; Guo, Y. G.; Wan, L. J. Lithium–sulfur batteries: Electrochemistry, materials, and prospects. *Angew. Chem., Int. Ed.* **2013**, *52*, 13186–13200.

[7] Liu, H.; Liu, M. Q.; Yang, L. Y.; Song, Y. L.; Wang, X. B.; Yang, K.; Pan, F. A bi-functional redox mediator promoting the ORR and OER in non-aqueous Li–O_2 batteries. *Chem. Commun.* **2019**, *55*, 6567–6570.

[8] Jiang, Z. P.; Jin, L.; Han, Z. L.; Hu, W.; Zeng, Z. Q.; Sun, Y. L.; Xie, J. Facile generation of polymer–alloy hybrid layers for dendrite-free lithium-metal anodes with improved moisture stability. *Angew. Chem., Int. Ed.* **2019**, *58*, 11374–11378.

[9] Wang, M. Q.; Peng, Z.; Luo, W. W.; Ren, F. H.; Li, Z. D.; Zhang, Q.; He, H. Y.; Ouyang, C. Y.; Wang, D. Y. Tailoring lithium deposition via an SEI-functionalized membrane derived from LiF decorated layered carbon structure. *Adv. Energy Mater.* **2019**, *9*, 1802912.

[10] Huang, Z. J.; Zhou, G. M.; Lv, W.; Deng, Y. Q.; Zhang, Y. B.; Zhang, C.; Kang, F. Y.; Yang, Q. H. Seeding lithium seeds towards uniform lithium deposition for stable lithium metal anodes. *Nano Energy* **2019**, *61*, 47–53.

[11] Kim, J. Y.; Liu, G. C.; Tran, M. X.; Ardhi, R. E. A.; Kim, H.; Lee, J. K. Synthesis and characterization of a hierarchically structured three-dimensional conducting scaffold for highly stable Li metal anodes. *J. Mater. Chem. A* **2019**, *7*, 12882–12892.

[12] Song, H. Y.; Chen, X. L.; Zheng, G. L.; Yu, X. J.; Jiang, S. F.; Cui, Z. M.; Du, L.; Liao, S. J. Dendrite-free composite Li anode assisted by ag nanoparticles in a wood-derived carbon frame. *ACS Appl. Mater. Interfaces* **2019**, *11*, 18361–18367.

[13] Zhao, F.; Zhou, X. F.; Deng, W.; Liu, Z. P. Entrapping lithium deposition in lithiophilic reservoir constructed by vertically aligned ZnO nanosheets for dendrite-free Li metal anodes. *Nano Energy* **2019**, *62*, 55–63.

[14] Qian, J.; Li, Y.; Zhang, M. L.; Luo, R.; Wang, F. J.; Ye, Y. S.; Xing, Y.; Li, W. L.; Qu, W. J.; Wang, L. L. et al. Protecting lithium/sodium metal anode with metal-organic framework based compact and robust shield. *Nano Energy* **2019**, *60*, 866–874.

[15] Liu, Q. Y.; Yang, G. J.; Liu, S.; Han, M.; Wang, Z. X.; Chen, L. Q. Trimethyl borate as film-forming electrolyte additive to improve high-voltage performances. *ACS Appl. Mater. Interfaces* **2019**, *11*, 17435–17443.

[16] Zheng, J. M.; Engelhard, M. H.; Mei, D. H.; Jiao, S. H.; Polzin, B. J.; Zhang, J. G.; Xu, W. Electrolyte additive enabled fast charging and stable cycling lithium metal batteries. *Nat. Energy* **2017**, *2*, 17012.

[17] Hu, Z. L.; Zhang, S.; Dong, S. M.; Li, Q.; Cui, G. L.; Chen, L. Q. Self-stabilized solid electrolyte interface on a host-free Li-metal anode toward high areal capacity and rate utilization. *Chem. Mater.* **2018**, *30*, 4039–4047.

[18] Yu, L.; Chen, S. R.; Lee, H.; Zhang, L. C.; Engelhard, M. H.; Li, Q. Y.; Jiao, S. H.; Liu, J.; Xu, W.; Zhang, J. G. A localized high-concentration electrolyte with optimized solvents and lithium difluoro(oxalate)borate additive for stable lithium metal batteries. *ACS Energy Lett.* **2018**, *3*, 2059–2067.

[19] Song, Y. L.; Yang, L. Y.; Zhao, W. G.; Wang, Z. J.; Zhao, Y.; Wang, Z. Q.; Zhao, Q. H.; Liu, H.; Pan, F. Revealing the short-circuiting mechanism of garnet-based solid-state electrolyte. *Adv. Energy Mater.* **2019**, *9*, 1900671.

[20] Wang, K.; Yang, L. Y.; Wang, Z. Q.; Zhao, Y.; Wang, Z. J.; Han, L.; Song, Y. L.; Pan, F. Enhanced lithium dendrite suppressing capability enabled by a solid-like electrolyte with different-sized nanoparticles. *Chem. Commun.* **2018**, *54*, 13060–13063.

[21] Zhang, X. K.; Xie, J.; Shi, F. F.; Lin, D. C.; Liu, Y. Y.; Liu, W.; Pei, A.; Gong, Y. J.; Wang, H. X.; Liu, K. et al. Vertically aligned and continuous nanoscale ceramic–polymer interfaces in composite solid polymer electrolytes for enhanced ionic conductivity. *Nano Lett.* **2018**, *18*, 3829–3838.

[22] Zhang, Y. B.; Chen, R. J.; Wang, S.; Liu, T.; Xu, B. Q.; Zhang, X.; Wang, X. Z.; Shen, Y.; Lin, Y. H.; Li, M. et al. Free-standing sulfide/polymer composite solid electrolyte membranes with high conductance for all-solid-state lithium batteries. *Energy Storage Mater.* **2020**, *25*, 145–153.

[23] Liang, X.; Wen, Z. Y.; Liu, Y.; Wu, M. F.; Jin, J.; Zhang, H.; Wu, X. W. Improved cycling performances of lithium sulfur batteries with $LiNO_3$-modified electrolyte. *J. Power Sources* **2011**, *196*, 9839–9843.

[24] Zhang, S. S. Role of $LiNO_3$ in rechargeable lithium/sulfur battery. *Electrochim. Acta* **2012**, *70*, 344–348.

[25] Xu, G. J.; Pang, C. G.; Chen, B. B.; Ma, J.; Wang, X.; Chai, J. C.; Wang, Q. F.; An, W. Z.; Zhou, X. H.; Cui, G. L. et al. Prescribing functional additives for treating the poor performances of high-voltage (5 V-class) $LiNi_{0.5}Mn_{1.5}O_4$/MCMB Li-Ion Batteries. *Adv. Energy Mater.* **2018**, *8*, 1701398.

[26] Zhang, X. Q.; Chen, X.; Cheng, X. B.; Li, B. Q.; Shen, X.; Yan, C.; Huang, J. Q.; Zhang, Q. Highly stable lithium metal batteries enabled by regulating the solvation of lithium ions in nonaqueous electrolytes. *Angew. Chem., Int. Ed.* **2018**, *57*, 5301–5305.

[27] Zhang, B. K.; Tan, R.; Yang, L. Y.; Zheng, J. X.; Zhang, K. C.; Mo, S. J.; Lin, Z.; Pan, F. Mechanisms and properties of ion-transport in inorganic solid electrolytes. *Energy Storage Mater.* **2018**, *10*, 139–159.

[28] Dong, T. T.; Zhang, J. J.; Xu, G. J.; Chai, J. C.; Du, H. P.; Wang, L. L.; Wen, H. J.; Zang, X.; Du, A. B.; Jia, Q. M. et al. A multifunctional polymer electrolyte enables ultra-long cycle-life in a high-voltage lithium metal battery. *Energy Environ. Sci.* **2018**, *11*, 1197–1203.

[29] Wang, C.; Wang, T.; Wang, L. L.; Hu, Z. L.; Cui, Z. L.; Li, J. D.; Dong, S. M.; Zhou, X. H.; Cui, G. L. Differentiated lithium salt design for multilayered PEO electrolyte enables a high-voltage solid-state lithium metal battery. *Adv. Sci.* **2019**, *6*, 1901036.

[30] Yang, L. Y.; Wang, Z. J.; Feng, Y. C.; Tan, R.; Zuo, Y. X.; Gao, R. T.; Zhao, Y.; Han, L.; Wang, Z. Q.; Pan, F. Flexible composite solid electrolyte facilitating highly stable "soft contacting" Li–electrolyte interface for solid state lithium-ion batteries. *Adv. Energy Mater.* **2017**, *7*, 1701437.

[31] Yue, L. P.; Ma, J.; Zhang, J. J.; Zhao, J. W.; Dong, S. M.; Liu, Z. H.; Cui, G. L.; Chen, L. Q. All solid-state polymer electrolytes for high-performance lithium ion batteries. *Energy Storage Mater.* **2016**, *5*, 139–164.

[32] Chai, J. C.; Liu, Z. H.; Zhang, J. J.; Sun, J. R.; Tian, Z. Y.; Ji, Y. Y.; Tang, K.; Zhou, X. H.; Cui, G. L. A superior polymer electrolyte with rigid cyclic carbonate backbone for rechargeable lithium ion batteries. *ACS Appl. Mater. Interfaces* **2017**, *9*, 17897–17905.

[33] Zhu, M.; Wu, J. X.; Wang, Y.; Song, M. M.; Long, L.; Siyal, S. H.; Yang, X. P.; Sui, G. Recent advances in gel polymer electrolyte for high-performance lithium batteries. *J. Energy Chem.* **2019**, *37*, 126–142.

[34] Liu, Y. Y.; Lin, D. C.; Li, Y. Z.; Chen, G. X.; Pei, A.; Nix, O.; Li, Y. B.; Cui, Y. Solubility-mediated sustained release enabling nitrate additive in carbonate electrolytes for stable lithium metal anode. *Nat. Commun.* **2018**, *9*, 3656.

[35] Shi, Q. W.; Zhong, Y. R.; Wu, M.; Wang, H. Z.; Wang, H. L. High-capacity rechargeable batteries based on deeply cyclable lithium metal anodes. *Proc. Natl. Acad. Sci. USA* **2018**, *115*, 5676–5680.

[36] Yan, C.; Yao, Y. X.; Chen, X.; Cheng, X. B.; Zhang, X. Q.; Huang, J. Q.; Zhang, Q. Lithium nitrate solvation chemistry in carbonate electrolyte sustains high-voltage lithium metal batteries. *Angew. Chem., Int. Ed.* **2018**, *57*, 14055–14059.

[37] Adams, B. D.; Zheng, J. M.; Ren, X. D.; Xu, W.; Zhang, J. G. Accurate determination of coulombic efficiency for lithium metal anodes and lithium metal batteries. *Adv. Energy Mater.* **2018**, *8*, 1702097.

[38] Zhou, Q.; Ma, J.; Dong, S. M.; Li, X. F.; Cui, G. L. Intermolecular chemistry in solid polymer electrolytes for high-energy-density lithium batteries. *Adv. Mater.* **2019**, *31*, 1902029.

[39] Rietman, E. A.; Kaplan, M. L.; Cava, R. J. Lithium ion-poly (ethylene oxide) complexes. I. Effect of anion on conductivity. *Solid State Ionics* **1985**, *17*, 67–73.

[40] Chen, T.; Kong, W. H.; Zhang, Z. W.; Wang, L.; Hu, Y.; Zhu, G. Y.; Chen, R. P.; Ma, L. B.; Yan, W.; Wang, Y. R. et al. Ionic liquid-immobilized polymer gel electrolyte with self-healing capability, high ionic conductivity and heat resistance for dendrite-free lithium metal batteries. *Nano Energy* **2018**, *54*, 17–25.

[41] Alpen, U. V.; Rabenau, A.; Talat, G. H. Ionic conductivity in Li_3N single crystals. *Appl. Phys. Lett.* **1977**, *30*, 621–623.